

Quantitative scoring of epithelial and mesenchymal qualities of cancer cells using machine learning and quantitative phase imaging

Van Kha Lam ^a, Thanh Nguyen ^b, Vy Bui ^b, Byung-Min Chung ^c, Lin-Ching Chang ^b, George Nehmetallah ^b, Christopher B. Raub ^a

^aThe Catholic University of America, Department of Biomedical Engineering, 620 Michigan Ave. NE, Washington, DC, USA, 20064

^bThe Catholic University of America, Department of Electrical Engineering and Computer Science, 620 Michigan Ave. NE, Washington, DC, USA, 20064

^cThe Catholic University of America, Department of Biology, 620 Michigan Ave. NE, Washington, DC, USA, 20064

Abstract

This study proposes a morphological score generated from machine learning to classify and grade cancer cells' phenotype on the epithelial-mesenchymal spectrum. To address this, cell phase maps from digital holography microscopy of two non-cancer epithelial and mesenchymal cell lines were trained and classified using several machine learning algorithms, with 96-100 % accuracy. After training, the models were transferred to classify two breast cancer cell lines, MCF-7 and MDA-MB-231, in which epithelial-mesenchymal characteristics are relevant to function. The proposed score is a robust approach for detecting unknown cancer cells based on epithelial-mesenchymal features and should be suitably applied to single-cell studies.

Introduction

Quantitative phase imaging (QPI) is a label-free optical imaging technique that measures the phase delay introduced when a coherent laser beam travels through a thin transparent specimen, such as cells ¹. The optical pathlength from QPI yields information about cell morphology, geometric thickness, refractive index which is relevant to protein concentration, subcellular organelles distribution and cell function ^{2, 3}. Hence, a collection of quantitative parameters from optical phase maps constitute a cell type's phase signature, providing additional information beyond the cell shape. Telecentric digital holographic microscopy (DHM) is a free-labelling and non-invasive QPI techniques acquiring low power density at the specimen, high temporal resolution, and rich quantitative pixel information that is well-suited to image biological specimens. Other key features of DHM include the ability to significantly reduce additional optical phase aberrations which are often introduced by an imaging objective ². Recent applications of DHM to the assessment of living biological specimens include characterization of the global morphology of confluent cell layers ⁴, analysis of cell proliferation and morphology on various substrates ^{1,5,6}, cell responses to drugs ^{7, 8}, determination of phase features relating to cell motility ^{9,10}, and cell classification in flow cytometry ^{11, 12}.

Quantitative phase imaging has great potential to evaluate cells in thin sections and in cell-based screening assays. In addition, machine learning applications to QPI include rapid evaluation and classification of cell types and (patho)physiological states ^{9,11-17}, and improvements in reconstructed image quality ^{18,19}, reviewed in ¹⁹. For example, machine learning classification from QPI compared favorably to manual scoring of the Gleason grade of prostate cancer from histology sections ²⁰, or to conventional screening in terms of predicting pathological features of hematological diseases ²¹. While single method like support vector machines (SVM) have been particularly successful in classification of cell lines using such quantitative phase parameters

^{9,12,22,23}, not many studies have reported about the use of ensemble method. In fact, ensemble methods can train multiple weak learners and combine them to obtain better predictive performance for classification. A recent study suggested that ensemble methods could improve detection of clear cell renal cell carcinoma in kidney disease leading to improved diagnosis and treatment ²⁴. Other studies also reported that QPI and machine learning could help pathologists and scientists to accurately detect circulating tumor cells ²⁵, classify cancer cells ^{26,27}, evaluate metastatic potential of cancer cells ²⁸, and assess cancer drug resistance ²⁹. With the potentials to save time, labor, and reduce human error in phenotypic profiling, machine learning-assisted QPI has great power to aid in interpreting large-scale and high-dimensionality data from cells, potentially enhancing cancer diagnosis and treatment.

A key aspect of cancer relevant to disease outcomes is cancer cell morphology. Many cancers adopt either epithelial or mesenchymal morphologies, dependent on certain gene mutations, gene expression profiles influenced by the microenvironment, and epigenetic changes ³⁰. Indeed, the route to transformation for many pre-cancers involves epithelial-to-mesenchymal transition, in which cells switch from a quiescent phenotype with rounded morphology to an actively motile, invasive phenotype with elongated morphology ^{31,32}. Complicating this picture, some cancer cell lines, such as MCF-7 cells, are rounded and form aggregates *in vitro*, yet are more invasive than cancer cell lines with single, elongated cell morphologies ³³. Another well-studied breast cancer cell line, MDA-MB-231, adopts both elongated, mesenchymal, and rounded, amoeboid morphologies as a bi-modal invasion strategy to overcome microenvironmental barriers ³⁴. In previous studies, support vector machines (SVM) were used to classify rounded and elongated MDA-MB-231 cells ⁵ and distinguish MCF-7 and MDA-MB-231 cells from non-cancer epithelial and mesenchymal cell lines ⁹. These studies raised the question of whether a universal score could be developed to grade cells along the spectrum of epithelial to mesenchymal features.

Since results from previous studies classified cells based on textural and shape-based phase map features, we hypothesized that a quantitative score from machine learning algorithms trained on non-cancer epithelial and mesenchymal cell lines could be used to assign mesenchymal or epithelial morphological status to cancer cells. To test this hypothesis, a binary classifier of two non-cancer gingival cell lines, one epithelial and one fibroblast/mesenchymal, was evaluated. Then, the algorithm trained on non-cancer cells was applied to two cancer cell lines of mixed morphology, and an epithelial-mesenchymal (EM) score was derived. Results indicate that such an approach accurately classifies epithelial and mesenchymal cell lines and assigns cancer cells a phenotypic score on the epithelial-mesenchymal axis consistent with observed morphology. We propose this approach of deriving morphological phenotypic scores from machine learning on archetypal cells as a generally useful and robust way to assess phenotypic characteristics of unknown cell populations and single cells which eventually is promising to both future clinical and research applications.

Materials and methods

Cell culture

Cell culture procedures were followed as in ⁹. For DHM imaging, cells were passaged when reaching 80-90% confluence and seeded on glass-bottomed petri dishes. Immortalized human gingival keratinocytes (Gie-No3B11, abbreviated as GIE, derived from buccal gingiva)³⁵, immortalized human gingival fibroblasts (HGF, derived from American Type Culture Collection

CRL-2014 primary gingival cells)^{36,37}, and the breast cancer cell lines MCF-7³⁸ and MDA-MB-231³⁹, both adenocarcinomas derived from pleural effusions, were seeded at respective densities 60,000 40,000 40,000 and 30,000 cells in a 35 mm diameter glass-bottomed Petri dish (Part #. 229632 CELLTREAT Scientific Products, Pepperell, Massachusetts, USA). The different densities were estimated to produce a roughly equal number of cells per field of view after 24 hours due to differences in growth rates and aggregation. Cancer cell lines were fed with Dulbecco's modified Eagle's medium (Lot # SLBW4140, Sigma-Aldrich, St. Louis, MO, USA), supplemented with 10% Fetalgro (Rocky Mountain Biologicals, Missoula, Montana) and 1% penicillin-streptomycin (Corning Inc., Corning, New York). The HGF and GIE cell lines were cultured in Prigrow 3 and Prigrow 4, respectively (Applied Biological Materials, Inc., British Columbia, Canada). Nutrient media for gingival cell lines were supplemented with 10% fetal bovine serum and 1% penicillin-streptomycin. When cells started to adhere after 24 hours, cells were fed with 200 μ l of fresh, pre-warmed media and were covered with sterile cover slips. In order to avoid effects on cells from the ambient environment, each imaging session was performed over 15-20 minutes of total time out of the incubator.

DHM set up, imaging and pre-processing

A detailed description of the telecentric DHM set-up and image processing was described in the following published studies which is reported to optically compensate for phase aberrations resulting to the ease of computational process^{2,5, 40}. The telecentric DHM setup (Fig. 1) is based on a bi-telecentric configuration that optically cancels the bulk of the spherical aberrations caused by the microscope objectives (MOs). The lateral resolution was 1.2 μ m with 0.18 μ m x 0.18 μ m pixel dimensions of the lateral reconstruction. A 632 nm wavelength HeNe laser was used to generate sample and reference beams that recombined at the camera sensor plane as holograms. The holograms were captured by a 1.3 MP CMOS camera (Lumenera Corporation, Inc., Ontario, Canada) and the reconstructed phase map was obtained using the Fresnel reconstruction algorithm².

Principal component analysis (PCA) was employed to cancel the main hologram phase aberrations. The following steps summarize the PCA algorithm: (a) Perform singular value decomposition (SVD) to obtain the first dominant PC, (b) obtain the linear and quadratic coefficients of the phase vectors from least square fitting of the two dominant singular vectors, (c) use these coefficients to compute the phase at the camera sensor, $\phi(k,l)$, and (d) multiply the conjugate $\phi^*(k,l)$ with the hologram to obtain $\exp[-j\phi_{ob}(k,l)]$, which is the phase due to the biological sample without contributions of MOs and tilt.

Machine learning and epithelial-mesenchymal score generation

Machine learning algorithms were evaluated and used to classify gingival cells and for transfer learning on cancer cells to define an epithelial-mesenchymal score (Fig. 2). Cells were segmented and seventeen phase parameters extracted from each of the four cell lines using a custom-written code in MATLAB (version R2015a) which was followed as in⁵⁹. Parameters are described in Supplemental Table S1. In total, there were 1,295 cells from four different cell lines which were segmented throughout this study including 332 cells of GIE, 309 cells of HGF, 307 cells of MCF-7 and 347 cells of MDA-MB-231.

Data were randomly partitioned at a ratio of 4:1 for training and testing. Training was performed on parameters from 252 and 229 GIE and HGF cells, respectively, following a five-fold cross validation. First, the 17 phase parameter predictors were transformed into principal components

(PCs) using PCA, and the PCA-transformed data used as inputs for training following five-fold cross-validation. Training and cross-validation using linear SVM was performed five times each, selecting 1 – 17 principal components as predictors. To evaluate the highest prediction accuracy during training, a one-factor ANOVA was performed for accuracy on a certain number of principal components used, with a Dunnett’s *post hoc* test to compare results to those of 1 principal component. Then, several single and ensemble methods were trained using the same number of PCs found to produce the highest accuracy from the linear SVM algorithm. Default settings in MATLAB were used for each classifier, including a cost parameter of 1 for misclassification. Accuracy was evaluated by comparing output labels to true cell line labels. These were compared to each other using a two-tailed Student’s *t*-test. Results were reported as the mean \pm standard deviation. Plots of the first two PCs and receiver operating characteristic curves for the best single and best ensemble method classifier were constructed.

These most accurate single and ensemble algorithms in training were exported as two models in the MATLAB workspace using the classificationLearner application. Each model was applied to the PCA-transformed data of 307 cells from MCF-7 and 347 cells from MDA-MB-231, combined with the 80 cells of GIE and 80 cells of the HGF cell lines used for testing. Besides the classification accuracy, SVM scores, Boosted Trees (AdaBoost) scores, Bagged Trees scores and SVM posterior probabilities, defined below, were also calculated. Cells from the two cancer cell lines MDA-MB-231 and MCF-7 were assigned as either “mesenchymal” or “epithelial”, based on the binary classifier. All scores and posterior probabilities were plotted in histograms to evaluate performance as an epithelial-mesenchymal score. In addition, SVM scores and posterior probabilities were correlated to determine the relative sensitivity of the score and probability throughout their respective ranges. The SVM score, s_j , the distance of the observation j to the decision boundary, was calculated as ⁴¹:

$$s_j = \left(\frac{x_j}{s_k} \right)' \beta + b \quad (1),$$

where x_j is the predictor data of observation j , $s_k = 2.5196$ is the linear kernel scale, β is the vector of fitted linear coefficients, and b is the intercept of the hyperplane defining the separation. The posterior probability, $P(s_j)$, was calculated as ⁴²:

$$P(s_j) = 1/(1 + \exp(As_j + B)) \quad (2),$$

where A and B are fitted slope and intercept, respectively, of the sigmoid function. Meanwhile, the prediction score for Adaboost, ranging from $-\infty$ to $+\infty$, was defined as ⁴³:

$$f(x) = \sum_{t=1}^T [a_t h_t(x)] \quad (3),$$

where $a_t = 0.5 \log((1 - \varepsilon_t)/\varepsilon_t)$ are weights of the sequential learners’ hypotheses, ε_t is the weighted classification error of learner t , $h_t(x)$ the prediction of learner t for prediction data x , for T total learners. The prediction scores for Boosted Trees are estimated posterior probabilities ⁴⁴,

$$\hat{P}_{bag}(c|x) = \sum_{t=1}^T [a_t \hat{P}_t(c|x) I(t \in S)] / \sum_{t=1}^T [a_t I(t \in S)] \quad (4),$$

where $\hat{P}_t(c|x)$ is the estimated posterior probability of learner t for class c given predictor data x , and $I(t \in S)$ is 1 when learner t is of the indices S from trees used in the prediction, else 0.

Results

Cell morphologies from optical phase maps vary across and within cell lines

Cell shapes from GIE (Fig. 3A) and HGF (Fig. 3D) cell lines resemble epithelial and mesenchymal morphologies, respectively. While GIE cells were more rounded and aggregated in clusters, HGF cells were more elongated with lower phase signals in pixels within the cell body. The cancer cell lines had morphologies in between GIE and HGF cells, with a more punctate phase texture (Fig. 3B and 3C). Cells from the MCF-7 cell line form epithelial-like clusters with sharp cell and cluster boundaries (Fig. 3B). Cells from the MDA-MB-231 cell line (Fig. 3C) appeared both rounded and elongated and were typically isolated.

Classification of epithelial and mesenchymal cell lines is highly accurate

Binary classification was evaluated for multiple algorithms available in the MATLAB machine learning and statistics toolbox, using the training set of 481 cell phase maps (n=252 from the GIE cell line, n=229 from the HGF cell line), all PCs as predictors, with accuracies ranging from 82 to 96%, and highest for linear SVM. Tuning the hyperparameters of box constraint level and kernel scale did not improve training accuracy. Therefore, the number of PCs used as predictors to linear SVM was varied from 1-17 (Table 1). Linear SVM with 6, 8, and 17 PCs all produced higher training accuracies than 1 PC (ANOVA, $F=47.6$, $p<0.001$, Dunnett's test vs. 1 PC, $p<0.001$). Six PCs were selected for use based on this statistical test and on previous models classifying cells based on phase features, which selected 6 PCs as the smallest number producing no increase in area under the curve of receiver operating characteristic curves. Linear SVM training resulted in an accuracy of $95.5\pm 0.3\%$. Training using SVMs with different kernel functions (quadratic, cubic, gaussian), decision trees, or $k=1$ nearest neighbor methods did not improve accuracy. The best ensemble method classifier was Bagged Trees (Bag ensemble method, 200 learners, and learning rate of 0.1), which did not further improve the accuracy than the best single method (t -test, $p=0.25$). Boosted trees (Adaboost algorithm, 200 learners, 0.1 learning rate) produced lower accuracy than linear SVM, each trained on 6 PCs (t -test, $p<0.01$). Figure 4(A-D) provides scatterplots of principal components 1 versus 2 and ROC curves for the best performing single and ensemble methods from model training and validation.

Testing based on the linear SVM and Bagged Trees models on a naive dataset of $n=80$ cells each from GIE and HGF cell lines produced error rates of 2.5-3.7% and 0%, respectively (Fig. 4E,F). Transfer learning using the linear SVM model classified 286/307 (87.0%) of MCF-7 cells as epithelial (GIE class), and 326/347 (93.9%) of MDA-MD-231 cells as mesenchymal (HGF class, data not shown). Transfer learning using the Bagged Trees model classified 262/307 (78.1%) of MCF-7 cells as epithelial (GIE class), and 329/347 (94.8%) of MDA-MD-231 cells as mesenchymal (HGF class, data not shown). Linear SVM, Bagged Trees, and Boosted Trees algorithms were used to calculate prediction scores for each cell of the test and transfer datasets (Fig. 5).

Binary epithelial-mesenchymal classifier prediction scores separate cancer cells by morphology

The distributions of prediction scores from linear SVM as Euclidean distance from the classifying hyperplane (Fig. 5A), posterior probabilities (Fig. 5B), Boosted Trees (Fig. 5C) and Bagged Trees (Fig. 5D) were evaluated. Histograms of linear SVM prediction scores (Fig. 5A, Eq. 1) produced the most normal distributions for test data of GIE and HGF, and transfer datasets of MCF-7 and MDA-MB-231 cells. Posterior probabilities from SVM (Fig. 5B, Eq. 2) and estimated posterior probabilities from Boosted Trees (Fig. 5C, Eq. 3) demonstrated excellent separation of classes but weighted toward 0 and 1. The Boosted Trees predictions produced bimodal distributions of MCF-7 and MDA-MB-231 cell scores (Fig. 5D, Eq. 4). Four scores from HGF cells were outliers, and so not included in the histograms. The outliers were extreme high SVM scores more than 5.6 standard deviations away from the population mean score. Correlations between linear SVM prediction scores versus posterior probabilities (Fig. 6A), and versus estimated posterior probabilities from Bagged Trees (Fig. 6B) were highly nonlinear for low and high scores of each. The correlation between linear SVM versus Boosted Trees prediction scores (Fig. 6C) was linear for central scores, but nonlinear overall, with discrete levels of Boosted Trees scores favored at low and high ends of the score range.

Cell phase maps representing the linear SVM (Fig. 7) and Boosted Trees (Fig. 8) prediction scores closest to minima, maxima, medians, and first and third quartiles demonstrated a graded appearance between epithelial and mesenchymal phenotypes, as represented by the cells nearest the median score from GIE and HGF cells, respectively (also depicted in Fig. 7 and 8). The selected cells are for the most part different (except for the MCF-7 Max and MDA-MB-231 Min, which were the same from the two scores) but reflect a trend of more mesenchymal morphology with higher score.

DISCUSSION

Machine learning algorithms applied to quantitative phase imaging of adherent cells in culture classify cell lines in a way useful for determining the functional phenotype on an epithelial-mesenchymal axis. This study proposes a transfer learning approach to define a graded phenotypic classification for breast cancer cells: train a binary classifier on known epithelial and mesenchymal cells, then test on the cancer cells of unknown phenotype, defining prediction scores for each unknown cell. The algorithms producing score distributions of cancer cells most evenly distributed between epithelial and mesenchymal extremes were linear SVM and Boosted Trees (AdaBoost) scores. The SVM score, the Euclidean distance to the linear hyperplane separating epithelial and mesenchymal classes, produced normal-appearing distributions within the cancer cell lines easily interpretable as lying along an epithelial-mesenchymal continuum. The Boosted Trees score also produced a prediction score able to be interpreted as an epithelial-mesenchymal continuum, but with bimodal score distributions for the cancer cell transfer learning predictions. These prediction scores from binary classifiers serve as robust, quantitative epithelial-mesenchymal scores to define unknown cells with morphologies blended in between two morphological extremes.

This proof-of-concept study has several strengths in design and analyses but also weaknesses related to the necessarily limited dataset. Strengths include the large numbers of cells imaged (>300 per cell line) and use of MCF-7 and MDA-MB-231 cell lines, well-characterized as being more epithelial and mesenchymal in nature, respectively. Quantitative phase imaging using DHM provides high accuracy of cell morphological measurements as well as pixel-level textural details^{5,9}. One potential concern is the consistency of the scoring results if different non-cancer epithelial and mesenchymal cells were used, instead of the gingival cells available for this study. The smooth

histogram in Fig.5A and graded appearance of cells from low to high scores in Fig. 7 and 8 increase confidence in the broad applicability of the developed scores. Still, a classifier trained on syngeneic non-cancer cells derived from the same tissue as the cancer would likely be more patient-specific. The bimodal nature of AdaBoost prediction scores for breast cancer cells (Fig. 5C) and granularity of AdaBoost scores at low and high ends of the range (Fig. 6B) are a weakness of the AdaBoost predictions compared to linear SVM prediction scores. This is explained by the iterative AdaBoost training algorithm that trains more learners on data that is harder to classify, i.e. is misclassified by initial learners in the ensemble method. The proposed epithelial-mesenchymal score requires validation with additional cancer cells of different epithelial and mesenchymal morphologies from various breast cancer subtypes⁴⁵. Despite these limitations to the current training and test datasets, the transfer learning method proposed here quantitatively sorts individual cells along a putative morphological axis that produces well-ranked cells by visual inspection, which common geometrical features including thickness, area and eccentricity were not incapable of (Fig. 7,8).

Morphological evaluation using an epithelial-mesenchymal score as proposed here could address a major issue in histology-based diagnostics deriving from cell to cell heterogeneity. Such heterogeneity, especially in the absence of specific molecular biomarkers, makes risk stratification, diagnosis and selection of treatment regimens less accurate⁴⁶. In phenotypic screening, DHM followed by assignment of a machine learning prediction score to individual cells would allow the detection of subtle morphological shifts in response to drug candidates, a task of increasing importance in drug discovery⁴⁷. Morphological evaluation is of potential utility in phenotypic screening and basic studies linking gene expression to phenotype and functional behavior. In this study, two breast cancer cell lines, MCF-7 and MDA-MB-231, were scored on an epithelial-mesenchymal axis by linear SVM, consistent with their morphological appearance. These cell lines are well known for appearing with clustered epithelial-type and single, mesenchymal-type morphologies, respectively due to differential expression of mesenchymal gene expression in MDA-MB-231 cells, including N-Cadherin, Snail, Slug, ZEB1 and 2, and Yes-associated protein 1 (YAP1)⁴⁸, or Snail, a transcription factor typical of mesenchymal cells, in MCF-7 cells⁴⁹. Such basic studies have potential impact in defining the roles of epithelial and mesenchymal phenotypes in cancer behavior, leading to a better understanding of phenotypic transitions and plasticity in cancer. An epithelial-mesenchymal score would aid such efforts by establishing the magnitude of phenotypic shifts with a given treatment.

An epithelial-mesenchymal score has utility in interpreting qualitative morphologic assignments. One exciting future development of such an approach would be to determine the sensitivity of the epithelial-mesenchymal score to differential expression of individual genes, something best achieved by direct comparison of parental and genetic knockout cell lines. There is some evidence that qualitative morphological classes do not correspond to invasiveness in all cases³³. This finding is consistent with at least a subset of genes being responsible for invasiveness but not aggregate morphology, a hypothesis which is testable through sequential genetic knockout, epithelial-mesenchymal scoring, and assessment of invasiveness *in vitro*. Quantitative phase imaging of cancer cells in functional assays combined with classification scores such as the proposed epithelial-mesenchymal score could aid such studies. In single cell studies, phase images of cells of interest could guide laser-capture microdissection to link observed behavior, morphology, and gene expression at a single cell level. Indeed, advanced machine learning techniques have recently been applied to isolate cell subpopulations based on phenotypic differences⁵⁰. The EM score concept described here could be applied to support decision making and actuation in intelligent cell sorting systems to determine the effects of cell heterogeneity⁵¹.

Significance of the work

This study proposes a concept of morphological score derived optical phase map and machine learning prediction score to sort unknown cancer cells along a recognizable morphological axis of a well-characterized epithelial and mesenchymal cell lines. This approach to sorting adherent cells has applications for phenotypic screening of cell lines exposed to drug candidates, as well as evaluating phenotype of unknown cells in a histological section derived from a cancer biopsy. Quantitative analyses proposed here can be applied to examine events in non-cancerous settings where epithelial versus mesenchymal cells play critical roles in development or wound healing⁵². A quantitative epithelial-mesenchymal score simplifies morphological evaluation and allows for future analysis of individual cells within a population to link cell phenotype, morphology, and gene expression.

Acknowledgement

This work was supported by the National Institute of Biomedical Imaging and Bioengineering (No. 1R03EB28017). The authors would like to thank Dr. Zaver Bhujwala (Johns Hopkins School of Medicine, Baltimore, MD) for the gift of the MDA-MB-231 cell line, and Drs. Diane Bienek and Gili Kaufman (Volpe Research Center, American Dental Association Foundation) for the gift of HGF and Gie-No3B11 cell lines. In addition, we thank Thuc Phan (Department of Electrical Engineering and Computer Sciences, CUA) for assistance with data collection using the DHM.

References

1. B. Kemper et al., "Label-free quantitative cell division monitoring of endothelial cells by digital holographic microscopy," *J. Biomed. Opt.* **15**(3), 036009-1–6 (2010) [doi:10.1117/1.3431712].
2. T. Nguyen et al., "Accurate quantitative phase digital holographic microscopy with single- and multiple-wavelength telecentric and nontelecentric configurations," *Appl. Opt.* **55**(21), 5666–5683 (2016) [doi:10.1364/ao.55.005666].
3. M. Born et al., "Interference and diffraction with partially coherent light," in *Principles of Optics*, pp. 554–632 (2013) [doi:10.1017/cbo9781139644181.019].
4. B. Kemper et al., "Quantitative phase imaging-based concepts for the analysis of global morphology changes in confluent cell layers," in *Proceedings Volume 10887, Quantitative Phase Imaging V*, p. 108871M (2019) [doi:10.1117/12.2509242].
5. V. K. Lam et al., "Quantitative assessment of cancer cell morphology and motility using telecentric digital holographic microscopy and machine learning," *Cytom. Part A* **93**(3), 334–345 (2018) [doi:10.1002/cyto.a.23316].
6. N. Pavillon et al., "Early cell death detection with digital holographic microscopy," *PLoS One* **7**(1), e30912 (2012) [doi:10.1371/journal.pone.0030912].
7. R. Cao et al., "Quantitative observations on cytoskeleton changes of osteocytes at different cell parts using digital holographic microscopy," *Biomed. Opt. Express* **9**(1), 72–85 (2018) [doi:10.1364/boe.9.000072].
8. Y. Li et al., "Digital holographic microscopy for longitudinal volumetric imaging of growth and treatment response in three-dimensional tumor models," *J. Biomed. Opt.* **19**(11), 116001-1–8 (2014) [doi:10.1117/1.jbo.19.11.116001].

9. V. K. Lam et al., “Machine Learning with Optical Phase Signatures for Phenotypic Profiling of Cell Lines,” *Cytom. Part A* **95**(7), 757–768 (2019) [doi:10.1002/cyto.a.23774].
10. D. Bettenworth et al., “Quantitative phase microscopy for evaluation of intestinal inflammation and wound healing utilizing label-free biophysical markers,” *Histol. Histopathol.* **33**(5), 417–432 (2018) [doi:10.14670/HH-11-937].
11. T. Blasi et al., “Label-free cell cycle analysis for high-throughput imaging flow cytometry,” *Nat. Commun.*, **7**:10256 (2016) [doi:10.1038/ncomms10256].
12. D. Roitshtain et al., “Quantitative phase microscopy spatial signatures of cancer cells,” *Cytom. Part A* **91**(5), 482–493 (2017) [doi:10.1002/cyto.a.23100].
13. Z. Han et al., “Breast Cancer Multi-classification from Histopathological Images with Structured Deep Learning Model,” *Sci. Rep.* **7**(4172) (2017) [doi:10.1038/s41598-017-04075-z].
14. D. A. Van Valen et al., “Deep Learning Automates the Quantitative Analysis of Individual Cells in Live-Cell Imaging Experiments,” *PLoS Comput. Biol.* **12**(11) (2016) [doi:10.1371/journal.pcbi.1005177].
15. C. L. Chen et al., “Deep Learning in Label-free Cell Classification,” *Sci. Rep.* **6**(21471) (2016) [doi:10.1038/srep21471].
16. Y. Rivenson et al., “PhaseStain: the digital staining of label-free quantitative phase microscopy images using deep learning,” *Light Sci. Appl.* **8**(23) (2019) [doi:10.1038/s41377-019-0129-y].
17. R. Li et al., “Deep Learning Segmentation of Optical Microscopy Images Improves 3-D Neuron Reconstruction,” *IEEE Trans. Med. Imaging* **36**(7), 1533–1541 (2017) [doi:10.1109/TMI.2017.2679713].
18. H. Wang, M. Lyu, and G. Situ, “eHoloNet: a learning-based end-to-end approach for in-line digital holographic reconstruction,” *Opt. Express* **26**(18), 22603–22614 (2018) [doi:10.1364/oe.26.022603].
19. Y. J. Jo et al., “Quantitative Phase Imaging and Artificial Intelligence: A Review,” *IEEE J. Sel. Top. Quantum Electron.* **25**(1) (2018) [doi:10.1109/JSTQE.2018.2859234].
20. E. Arvaniti et al., “Automated Gleason grading of prostate cancer tissue microarrays via deep learning,” *Sci. Rep.* **8**(12054) (2018) [doi:10.1038/s41598-018-30535-1].
21. G. Kim et al., “Learning-based screening of hematologic disorders using quantitative phase imaging of individual red blood cells,” *Biosens. Bioelectron.* **123**, 69–76 (2019) [doi:10.1016/j.bios.2018.09.068].
22. T. C. Nguyen et al., “Quantitative assessment of cancer cell morphology and movement using telecentric digital holographic microscopy,” in *Quantitative Phase Imaging III*, p. 100740U (2017) [doi:10.1117/12.2256128].
23. Y. Ozaki et al., “Label-free classification of cells based on supervised machine learning of subcellular structures,” *PLoS One* **14**(1), e0211347 (2019) [doi:10.1371/journal.pone.0211347].

24. K. H. Park et al., “Efficient Ensemble Methods for Classification on Clear Cell Renal Cell Carcinoma Clinical Dataset,” in *Lecture Notes in Computer Science (including subseries Lecture Notes in Artificial Intelligence and Lecture Notes in Bioinformatics)* (2018) [doi:10.1007/978-3-319-75420-8_22].
25. S. D.K. et al., “Label-free fingerprinting of tumor cells in bulk flow using inline digital holographic microscopy,” in *Biomedical Optics Express* **8**(2), pp. 536–554 (2017) [doi:10.1364/BOE.8.000536 LK - http://elinks.library.upenn.edu/sfx_local?sid=EMBASE&issn=21567085&id=doi:10.1364%2FBOE.8.000536&atitle=Label-free+fingerprinting+of+tumor+cells+in+bulk+flow+using+inline+digital+holographic+microscopy&stitle=Biomed.+Opt.+Express&title=Biomedical+Optics+Express&volume=8&issue=2&spage=536&epage=554&aulast=Singh&aufirst=Dhananjay+Kumar&auinit=D.K.&aufull=Singh+D.K.&coden=&isbn=&pages=536-554&date=2017&auinit1=D&auinitm=K].
26. S. Hakim, M. Yamaguchi, and F. Kimura, “Application of digital holography on diagnosis of malignant lymphoma,” in *14th Workshop on Information Optics, WIO 2015* (2015) [doi:10.1109/WIO.2015.7206908].
27. J. Mangal et al., “Unsupervised organization of cervical cells using bright-field and single-shot digital holographic microscopy,” *J. Biophotonics* **12**(8), e201800409 (2019) [doi:10.1002/jbio.201800409].
28. V. L. Calin et al., “Evaluation of the metastatic potential of malignant cells by image processing of digital holographic microscopy data,” *FEBS Open Bio* **7**(10), 1527–1538 (2017) [doi:10.1002/2211-5463.12282].
29. T. Yao et al., “An optical study of drug resistance detection in endometrial cancer cells by dynamic and quantitative phase imaging,” *J. Biophotonics* **12**(7), e201800443 (2019) [doi:10.1002/jbio.201800443].
30. P. A. Kenny et al., “The morphologies of breast cancer cell lines in three-dimensional assays correlate with their profiles of gene expression,” *Mol. Oncol.* **1**(1), 84–96 (2007) [doi:10.1016/j.molonc.2007.02.004].
31. J. P. Thiery, “Epithelial–mesenchymal transitions in tumour progression,” *Nat. Rev. Cancer* **2**(6), 442–454 (2002) [doi:10.1038/nrc822].
32. J. Zavadil et al., “Epithelial-mesenchymal transition,” in *Cancer Research* **68**(23), pp. 9574–9577 (2008) [doi:10.1158/0008-5472.CAN-08-2316].
33. M. J. Ziperstein, A. Guzman, and L. J. Kaufman, “Breast cancer cell line aggregate morphology does not predict invasive capacity,” *PLoS One* **10**(9), e0139523 (2015) [doi:10.1371/journal.pone.0139523].
34. K. Paňková et al., “The molecular mechanisms of transition between mesenchymal and amoeboid invasiveness in tumor cells,” *Cell. Mol. Life Sci.* **67**(1), 63–71 (2010) [doi:10.1007/s00018-009-0132-1].
35. S. Gröger, J. Michel, and J. Meyle, “Establishment and characterization of immortalized human gingival keratinocyte cell lines,” *J. Periodontal Res.* **43**(6), 604–614 (2008) [doi:10.1111/j.1600-0765.2007.01019.x].

36. S. Vardar-Sengul et al., “Expression Profile of Human Gingival Fibroblasts Induced by Interleukin-1 β Reveals Central Role of Nuclear Factor-Kappa B in Stabilizing Human Gingival Fibroblasts During Inflammation,” *J. Periodontol.* **80**(5), 833–849 (2009) [doi:10.1902/jop.2009.080483].
37. R. P. Illeperuma et al., “Immortalized gingival fibroblasts as a cytotoxicity test model for dental materials,” *J. Mater. Sci. Mater. Med.* **23**(3), 753–762 (2012) [doi:10.1007/s10856-011-4473-6].
38. H. D. Soule et al., “A human cell line from a pleural effusion derived from a breast carcinoma 1 , 2,” *J. Natl. Cancer Inst.* **51**(5), 1409–1416 (1973) [doi:10.1093/jnci/51.5.1409].
39. R. Cailleau et al., “Breast tumor cell lines from pleural effusions,” *J. Natl. Cancer Inst.* **53**(3), 661–674 (1974) [doi:10.1093/jnci/53.3.661].
40. C. Zuo et al., “Phase aberration compensation in digital holographic microscopy based on principal component analysis,” *Opt. Lett.* **38**(10), 1724–1726 (2013) [doi:10.1364/ol.38.001724].
41. J. S. Nello Cristianini, “An Introduction to Support Vector Machines and Other Kernel-based Learning Methods,” *Kybernetes* **22**(2) (2000).
42. J. C. Platt, “Probabilistic Outputs for Support Vector Machines and Comparisons to Regularized Likelihood Methods,” in *Advances in Large Margin Classifiers* (2000).
43. J. H. Friedman, “Greedy function approximation: A gradient boosting machine,” *Ann. Stat.* (2001).
44. L. Breiman, “Bagging predictors,” *Mach. Learn.* (1996).
45. X. Dai et al., “Breast cancer cell line classification and Its relevance with breast tumor subtyping,” *J. Cancer* **8**(16), 3131–3141 (2017) [doi:10.7150/jca.18457].
46. G. R. Sant, K. B. Knopf, and D. M. Albala, “Live-single-cell phenotypic cancer biomarkers-future role in precision oncology?,” *npj Precis. Oncol.* **1**(21) (2017) [doi:10.1038/s41698-017-0025-y].
47. W. Zheng, N. Thorne, and J. C. McKew, “Phenotypic screens as a renewed approach for drug discovery,” *Drug Discov. Today* **18**(21–22), 1067–1073 (2013) [doi:10.1016/j.drudis.2013.07.001].
48. A. Sulaiman et al., “Dual inhibition of Wnt and Yes-associated protein signaling retards the growth of triple-negative breast cancer in both mesenchymal and epithelial states,” *Mol. Oncol.* **12**(4), 423–440 (2018) [doi:10.1002/1878-0261.12167].
49. R. Mezencev et al., “Snail-induced epithelial-to-mesenchymal transition of MCF-7 breast cancer cells: Systems analysis of molecular changes and their effect on radiation and drug sensitivity,” *BMC Cancer* **16**(236) (2016) [doi:10.1186/s12885-016-2274-5].
50. C. Brasko et al., “Intelligent image-based in situ single-cell isolation,” *Nat. Commun.* **9**(226) (2018) [doi:10.1038/s41467-017-02628-4].
51. N. Nitta et al., “Intelligent Image-Activated Cell Sorting,” *Cell* **175**(1), 266–276 (2018) [doi:10.1016/j.cell.2018.08.028].

52. S. Lamouille, J. Xu, and R. Derynck, “Molecular mechanisms of epithelial-mesenchymal transition,” *Nat. Rev. Mol. Cell Biol.* **15**(3), 178–196 (2014) [doi:10.1038/nrm3758].

Figures and table

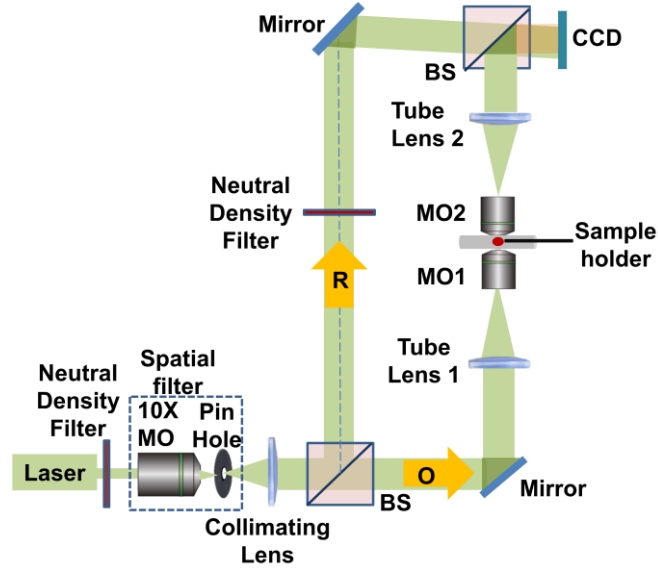


Fig. 1 The bi-telecentric digital holographic microscope in transmission configuration, including microscope objective (MO), beamsplitters (BS), object beam (O), reference beam (R) and CMOS camera.

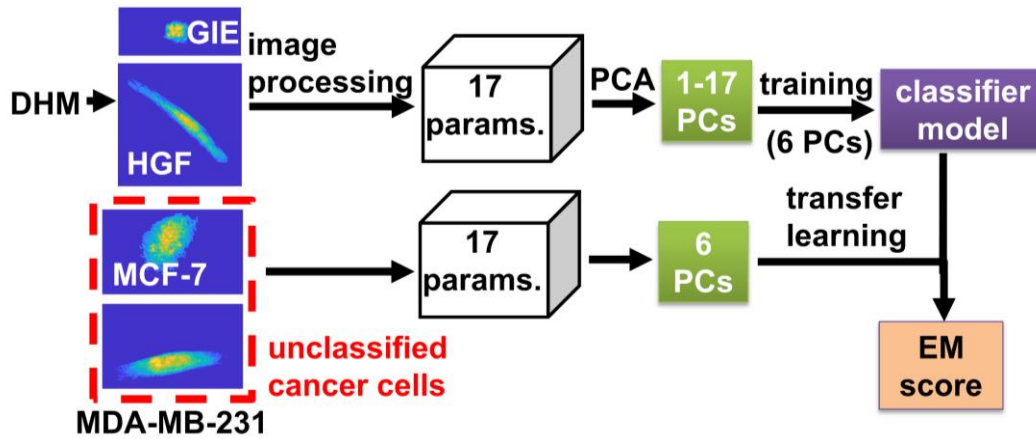


Fig. 2 Machine learning was performed on 1-17 features derived from phase maps reconstructed from adherent cells' holograms. Derived features from epithelial (GIE) and mesenchymal (HGF) cell types were used for training. For transfer learning, six principle components representing most of the variation in cell phase maps from two untrained cancer cell lines, MCF-7 and MDA-MB-231, were used for testing and to generate machine learning prediction scores as candidates for an epithelial-mesenchymal score.

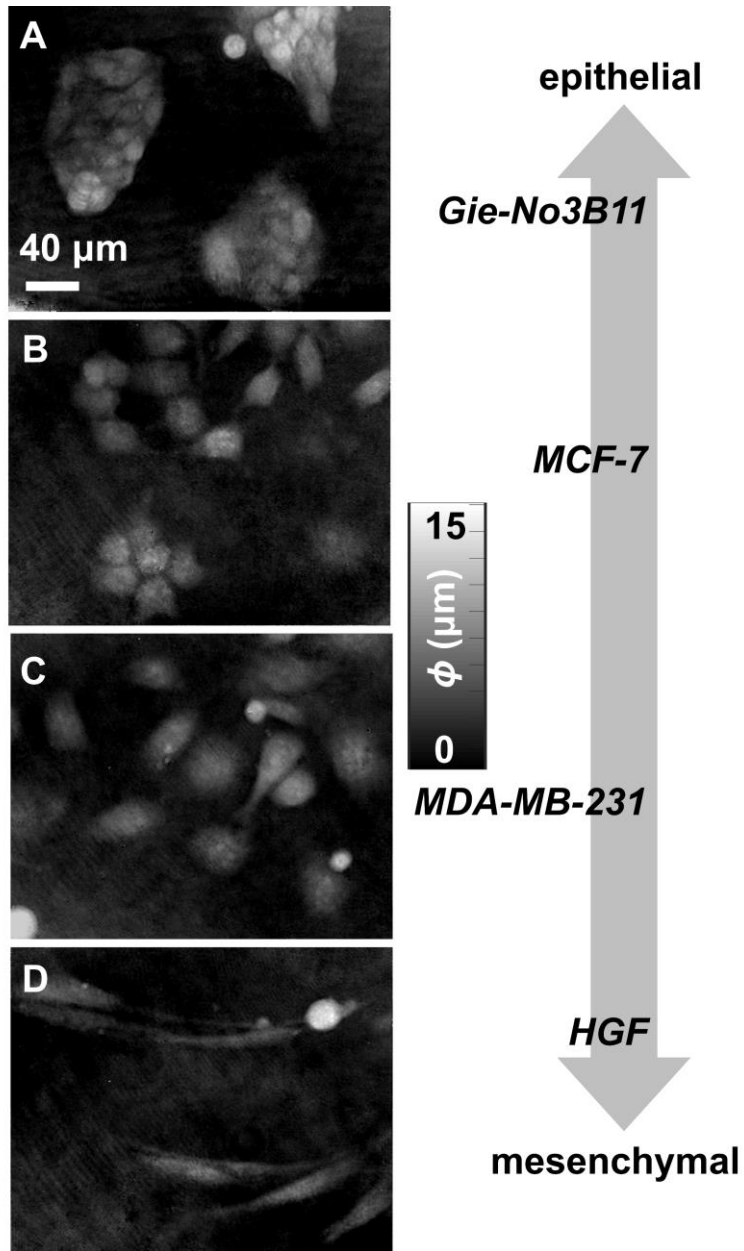


Fig. 3 Representative DHM phase maps from living, adherent cells of (A) Gie-No3B11 (GIE), (B) MCF-7, (C) MDA-MB-231, (D) HGF cell lines. The cells are ordered qualitatively on an epithelial-mesenchymal axis based on cell morphology apparent in phase maps. Scale and phase bars are indicated.

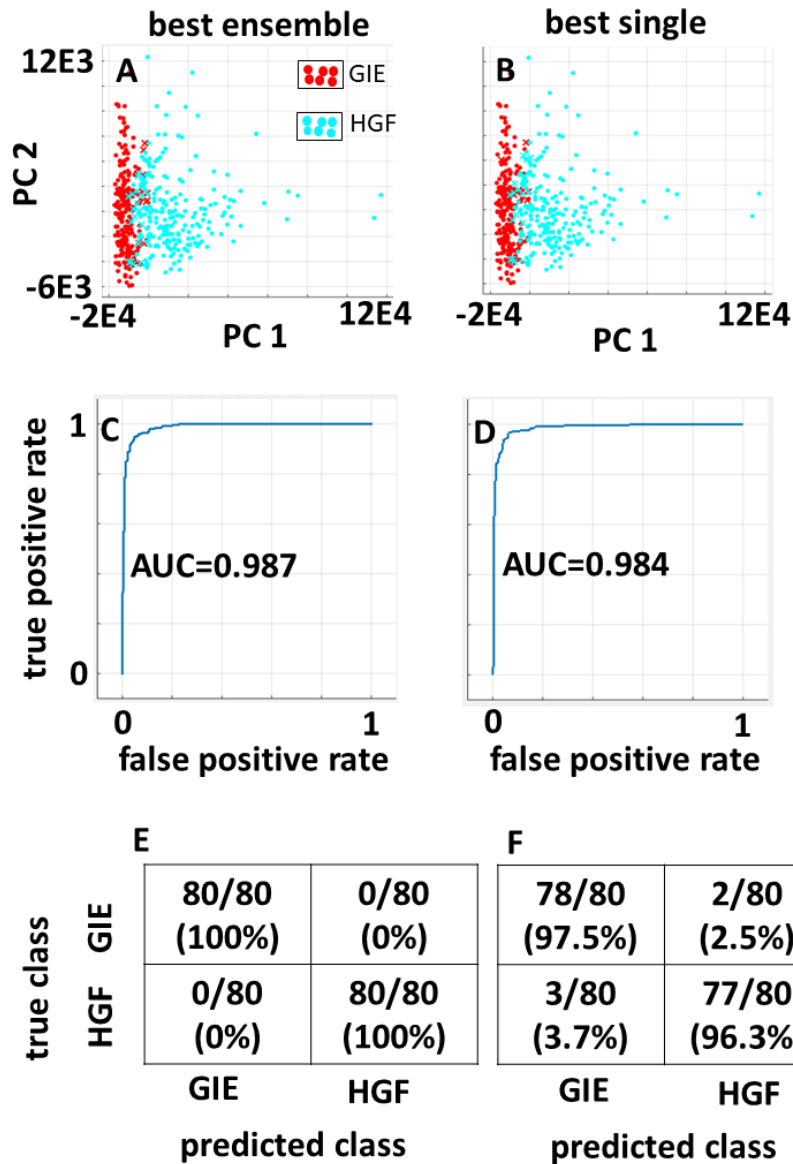


Fig. 4 Binary classifier training data (A,B) scatterplots of principal component (PC) 1 versus 2, highlighting correctly classified GIE (red circle) and HGF (cyan circle) cells, and misclassified cells (red and cyan x's, with color representing the true class). (C,D) Receiver operating characteristic curves from training data, with area under the curve (AUC) listed. (E-F) Error tables from a test dataset for (E) Bagged Trees, and (F) linear SVM.

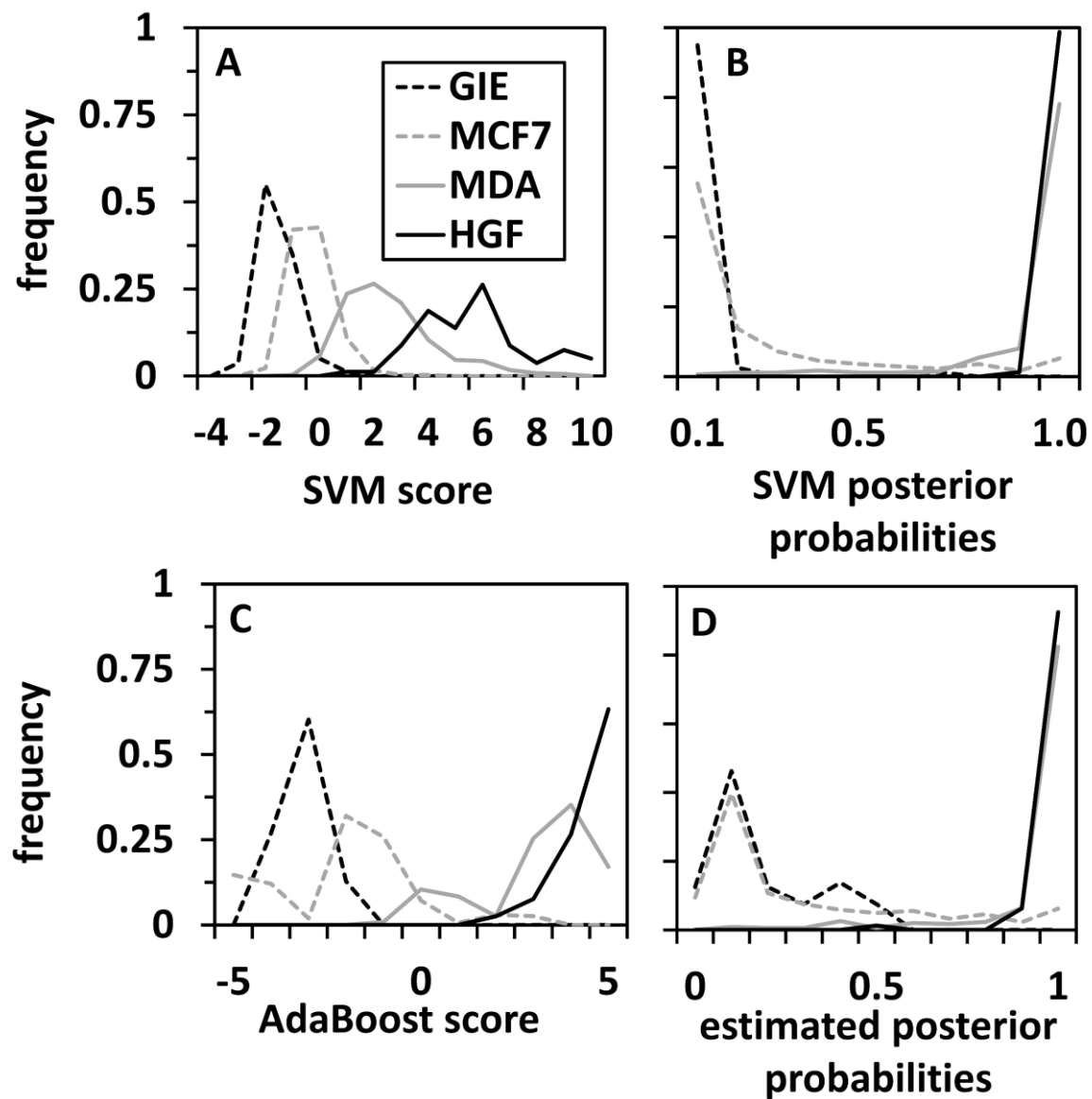


Fig. 5 Prediction scores for transfer learning of an epithelial-mesenchymal classifier to cancer cells. Histograms of prediction score distributions for (A) SVM predictions, (B) SVM posterior probabilities, (C) AdaBoost predictions, and (D) estimated posterior probabilities from Boosted Trees, for test datasets of $n=80$ GIE cells (black dashed line) and $n=80$ HGF cells (black solid line), and transfer learning datasets of $n=307$ MCF-7 cells (gray dashed line) and $n=347$ MDA-MB-231 cells (gray solid line).

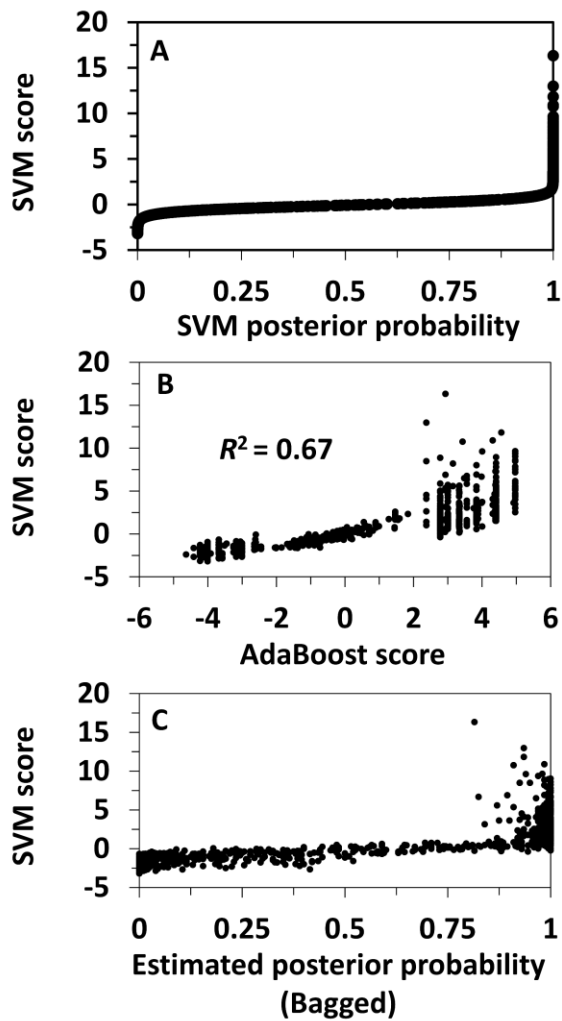


Fig. 6 Correlation plots of linear SVM prediction scores versus (A) posterior probability scores from SVM, (B) AdaBoost prediction scores, and (C) estimated posterior probability scores from Bagged Trees, for the dataset of 814 cells defined previously from GIE, HGF, MCF-7 and MDA-MB-231 cell lines.

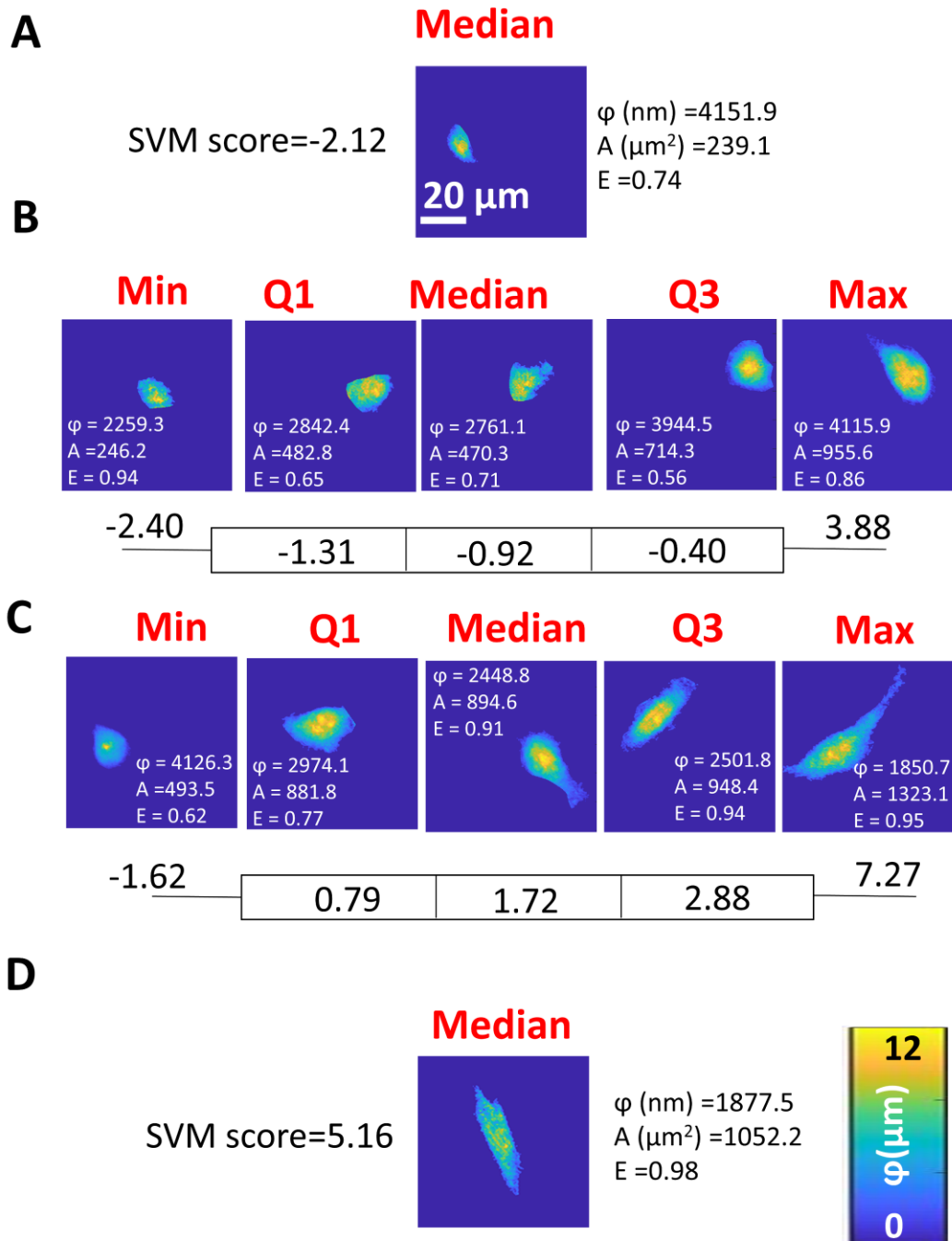


Fig. 7 Phase maps of epithelial, mesenchymal, and breast cancer cells representing the median SVM score of normal cell line (A) GIE and (D) HGF. The minimum, first quartile, median, second quartile, and maximum SVM score for cancer cell lines of (B) MCF-7 and (C) MDA-MB-231. SVM scores were derived from a binary classification SVM model trained on GIE and HGF cells, then tested on breast cancer cells to generate weighted classification scores. Phase height (ϕ) in nm, area (A) in μm^2 and eccentricity (E) generated by DHM were listed in each cell map.

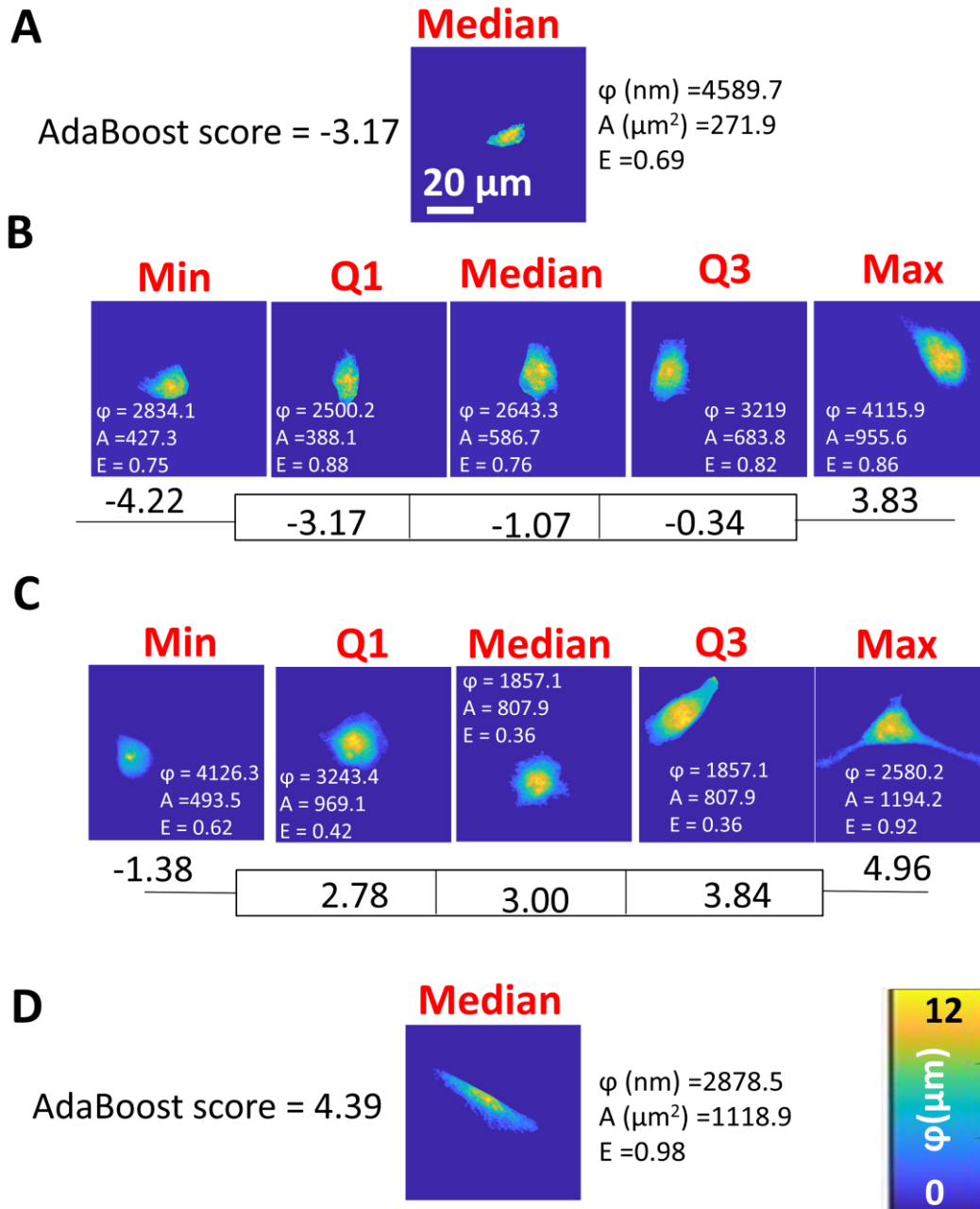


Fig. 8 Phase maps of epithelial, mesenchymal, and breast cancer cells representing the median AdaBoost score of normal cell line (A) GIE and (D) HGF. The minimum, first quartile, median, second quartile, and maximum AdaBoost score for cancer cell lines of (B) MCF-7 and (C) MDA-MB-231. AdaBoost scores were derived from a binary classification AdaBoost model trained on GIE and HGF cells, then tested on breast cancer cells to generate weighted classification scores. Phase height (ϕ) in nm, area (A) in μm^2 and eccentricity (E) generated by DHM were listed in each cell map.

Table 1 Training accuracy of various machine learning algorithms to classify epithelial and mesenchymal cells.

type	method	accuracy (%, $\mu \pm SD$)
single	Linear SVM, 1 PC	93.0 \pm 0.2
	Linear SVM, 2 PCs	93.0 \pm 0.2
	Linear SVM, 4 PCs	92.8 \pm 0.3
	Linear SVM, 5 PCs	93.4 \pm 0.6
	Linear SVM, 6 PCs*	95.5 \pm 0.3
	Linear SVM, 8 PCs*	95.1 \pm 0.3
	Linear SVM, 17 PCs*	95.2 \pm 0.6
	Other SVMs, 6 PCs	95.4 \pm 3.9
	Decision trees, 6 PCs	91.6 \pm 0.2
	Nearest Neighbor, 6 PCs	88.9 \pm 3.7
ensemble	Boosted Trees, 6 PCs, Adaboost**	94.3 \pm 0.5
	Bagged Trees, 6 PCs, Bag	95.2 \pm 0.4

PCs, principal components; SVM, support vector machines

* $p < 0.001$, ANOVA and *post hoc* Dunnett's test vs. linear SVM, 1 PC

** $p < 0.001$, Student's *t*-test, vs. linear SVM, 6 PCs

Table S1. List of 17 cell parameters generated from DHM segmentation using a written Matlab code

μ	CellMean	Average phase height	32-bit full, in nm	$\mu = \frac{1}{N} \sum_{i=1}^N x_i$
SD	CellStd	Phase height standard deviation	32-bit full, in nm	$SD = \sqrt{\frac{1}{N-1} \sum_{i=1}^N A_i - \mu ^2}$
ku	Kurt	Phase height kurtosis	32-bit full	$k = \frac{E(x - \mu)^4}{\sigma^4}$
sk	Skew	Phase height skewness	32-bit full	$sk = \frac{E(x - \mu)^3}{\sigma^3}$
Ar	Stats.Area	Segmented cell area	Units of pixels	--
Per	Stats.Eccentricity	Segmented cell fit ellipse eccentricity	Units of pixels	--
Ecc	Stats.Perimeter	Segmented cell perimeter	Units of pixels	--
Co	Stats2.Contrast	2 nd order texture parameter	8-bit scaled	$\sum_{i,j} i - j ^2 p(i, j)$
Cor	Stats2.Correlation	2 nd order texture parameter	8-bit scaled	$\sum_{i,j} \frac{(i - \mu_i)(j - \mu_j)p(i, j)}{\sigma_i \sigma_j}$
En	Stats2.Energy	2 nd order texture parameter	8-bit scaled	$\sum_{i,j} p(i, j)^2$
Hm	Stats2.Homogeneity	2 nd order texture parameter	8-bit scaled	$\sum_{i,j} \frac{p(i, j)}{1 + i - j }$
μ_n	Nucleus mean	Average nucleus phase height	32-bit full, in nm	See Cell Mean
μ_{nm}	Nucleus maximum mean	Maximum nucleus phase height	32-bit full, in nm	--
a	Nucleus area	Segmented nucleus area	Units of pixels	--
sd	Nucleus Std	Nucleus phase height standard deviation	32-bit full, in nm	See Cell Standard Deviation
k_n	Nucleus kurtosis	Phase height kurtosis	32-bit full	See kurtosis
sk_n	Nucleus skew	Phase height skewness	32-bit full	See skew